How multiscale approaches can benefit the design of cellular rockfall protection structure

Franck Bourrier, Stéphane Lambert, A. Heymann, P. Gotteland, François Nicot

How multi-scale approaches can benefit the design of cellular rockfall protection structures

F. Bourrier. Cemagref, UR EMGR - 3SR, UMR5521, DU Grenoble Universités, 2, rue de la papeterie, BP 76, 38402 St-Martin d'Hères CEDEX, France.
S. Lambert. Cemagref, UR ETGR, 2, rue de la papeterie, BP 76, 38402 St-Martin d'Hères CEDEX, France.
A. Heymann. Cemagref, UR ETGR - 3SR, UMR5521, DU Grenoble Universités - Razel, Groupe Fayat, 2, rue de la papeterie, BP 76, 38402 St-Martin d'Hères CEDEX, France.
P. Gotteland. 3SR, UMR5521, DU Grenoble Universités, rue de la Piscine, 38041 CEDEX 9, Grenoble, France.
F. Nicot. Cemagref, UR ETGR, 2, rue de la papeterie, BP 76, 38402 St-Martin d'Hères CEDEX, France.

Abstract: Cellular structures are efficient technological solutions for rockfall protection. A multi-scale approach is used to develop a cellular rockfall protection structure model for engineering purposes. The macroscopic structure is composed of mesoscale individual layers made up of rocky particles contained in wire netting cages, fine granular material, and a reinforced embankment. Simple constitutive models were developed for the different mesoscale layers of the structure. Information is gathered from experiments at the layer scale to calibrate the parameters of the constitutive models. The capacities of the model are evaluated by comparisons between simulations and impact experiments on small structures. Despite quantitative differences, the comparative analysis highlights that the structure model can account for the main physical mechanisms occurring during the impact on sandwich structures. This analysis also emphasizes the model's applicability for engineering purposes.

Key words: multi-scale modelling, rockfall, protective structures, design, impact modelling, cellular structures, gabions.

Résumé : Les structures cellulaires sont une solution technologique efficace pour la protection contre les éboulements. Une approche multi-échelles est utilisée pour développer un modèle de structures cellulaires pour la protection contre les éboulements pour des fins d'ingénierie. La structure macroscopique est constituée de couches individuelles à l'échelle méso faites de particules rocheuses contenues dans des cages de fils métalliques, du matériel granulaire fin et un remblai renforcé. Des modèles constitutifs simples ont été développés pour les différentes couches à l'échelle méso de la structure. Des données provenant d'essais réalisés à l'échelle de la couche ont été utilisées pour calibrer les paramètres des modèles constitutifs. Les capacités du modèle sont évaluées en comparant les résultats des simulations à ceux des essais sur des petites structures. Malgré les différences au niveau quantitatif, l'analyse comparative révèle que le modèle de structure peut simuler les principaux mécanismes physiques se produisant lors d'impacts sur des structures étagées. Cette analyse démontre aussi l'applicabilité du modèle pour des fins d'ingénierie.

Mots-clés : modélisation multi-échelle, éboulement, structures de protection, conception, modélisation des impacts, structures cellulaires, gabions.

Introduction

In the field of civil engineering, soil structures are sometimes designed to withstand localized impact loadings resulting from projectiles, vehicle crashes or falling rocks. In the case of falling rocks, the aim can be either to protect a buried structure (Pichler et al. 2005) or to create an impassable obstacle in the rock's trajectory (Peila et al. 2007). This barrier function is often provided by a reinforced soil levee or embankment. Despite several past experimental and numerical studies (Hearn et al. 1995; Yoshida 1999; Blovsky 2002; Peila et al. 2002; Carotti et al. 2004; Aminata et al. 2008; Ronco et al. 2009; Plassiard and Donzé 2010), the design of these embankments generally stems from an empirical approach, based mainly on static equivalent loadings (Jaecklin 2006). Several analytical approaches for the design of these structures have also been developed based on a comparison between the braking force associated with the boulder and the shearing force associated with the embankment (see, for instance, Tissières 1999). Such approaches generally lead to the designing of massive rockfall protection structures, a problem for land occupancy reasons. A thorough analysis of the mechanical response of these structures remains to be done to improve their design, fully taking into account the dynamics associated with the loadings.

Numerical simulations have been performed to account for the complexity of the impact on embankments (Burroughs et al. 1993; Hearn et al. 1995; Peila et al. 2002, 2007; Carotti et al. 2004; Sung et al. 2007; Ronco et al. 2009; Plassiard and

Donzé 2010). These approaches obtained fair agreement with real-scale experimental results (Burroughs et al. 1993; Peila et al. 2002; Sung et al. 2007). Relevant information to account for the dynamic response of the structure may also be found in research on real-scale impact experiments on soil layers (Pichler et al. 2005) and gravel materials laid on rigid bases (Labiouse et al. 1994; Montani Stoffel 1998; Calvetti et al. 2005; Schellenberg et al. 2008).

With the aim of improving the efficiency of rockfall protection structures and reducing their overall size, an intensive research program was initiated — the Rempare project, funded by the French National Research Agency (ANR; project number ANR-06-rgcu-009-01). The main objectives of this project were to develop innovative rockfall protection structures and improve the methodologies used for the design of rockfall protection structures. Reinvestigating the principle of a sandwich structure, first pioneered in this domain by Yoshida (1999), the proposed solution consists of a structure built using cells filled with different materials (Fig. 1). The cellular structure is composed of several layers: a front layer subjected to the localized impact by the rock, coupled to a kernel layer aiming at dissipating the energy, and a back part that maintains stability and increases rigidity of the structure. The cells considered in this study are parallelepiped-like wire netting cages (or gabions). The front-layer cells are filled with a crushed quarry limestone. Finer fill material used for the kernel layer can either be sand or sand mixed with scrapped tires (Gotteland et al. 2005). Finally, the back part can be either a rigid concrete wall or a small embankment. The different scales from the constitutive materials to the structure were investigated in this research program, combining experiments with numerical modelling (Bertrand et al. 2005; Nicot et al. 2007; Lambert et al. 2009).

The present study aims at providing a practical design tool for rockfall protection cellular structures based on new experimental data and following a multi-scale approach. Multi-scale approaches consist of collecting information at the microscopic and mesoscopic scales, to define a model that can be used at the macroscopic scale. Multi-scale approaches, therefore, make it possible to investigate the response of a structure on a macroscopic scale by accounting for the determinant properties of constitutive materials at both microscopic and mesoscopic scales. In this study, the microscopic scale corresponds to the size of the particles of the constitutive materials, the mesoscopic scale is associated with each layer, and the macroscopic scale corresponds to the structure scale.

The approach consists of defining constitutive models for each layer based on experimental results at the mesoscopic scale, to combine these models and define a macroscopic structure model. The principle of the structure model is presented first. Then, the calibration of the constitutive models for the front layer is discussed. Finally, comparisons between impact simulations and experimental results for impacts on a small structure are used to study the influence of the properties of the kernel layer.

Numerical model

Principle of the structure model

The first objective of modelling the structure was to account for the discrete nature of a cellular structure, modelled as an assembly of elementary cells. Second, the aim was to build a model that could easily be used as a decision-making tool for engineering purposes. To achieve these objectives, a model based on the discrete element method (Cundall and Strack 1979), naturally accounting for the discrete nature of the structure, was developed. Rather than a continuous alternative method, such as a finite element method, this type of model also accounts for the large strains that are likely to occur within the structure and for the discontinuous displacements between the cells.

Fig. 1. Sandwich structures for rockfall protection: (*a*) embankment type and (*b*) wall type.

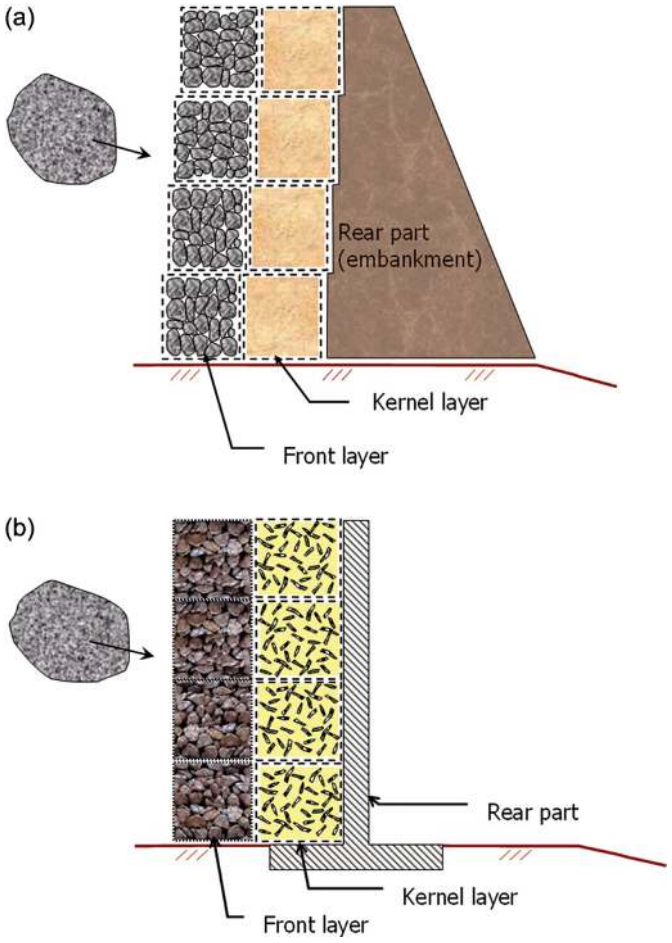

The structure described in the previous section is modelled as an assembly of cells. The geometries of the front and kernel layers are explicitly modelled, whereas the back part embankment is considered an elastic boundary condition. The front and kernel layers are divided into cells the same size as the front layer geocells (50 cm × 50 cm × 50 cm). The front and upper sides of the structure are assumed to be free to deform. The lower face of the structure lies directly on the soil, and is assumed to be rigid, with no additional anchorage. The lateral boundaries of the structure can either be free to deform or rigid.

The structure is replaced by a mesh of nodes located at the gravity centre of the cells (Fig. 2). The mass of each cell is concentrated at the node location. The different nodes interact with each other by remote interactions. The impacting

Fig. 2. (*a*) Three-dimensional view and (*b*) top view of the cellular structure model. Cube ridges are fictitious.

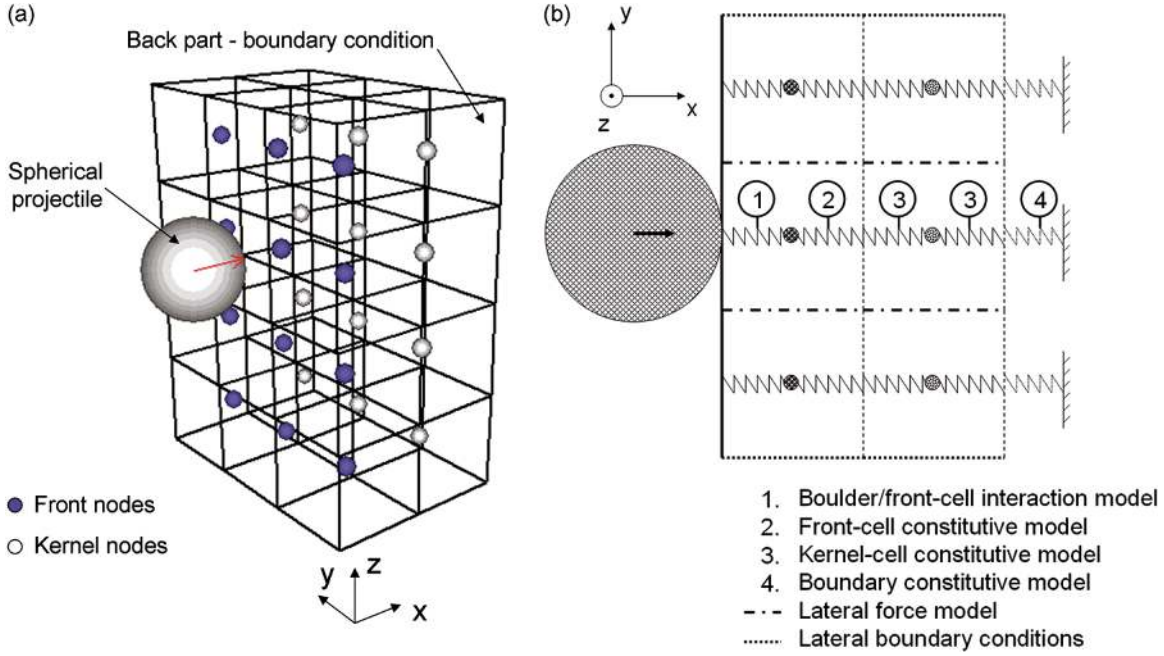

boulder is modelled as a sphere interacting with the nodes associated with the front-layer cells by remote interactions.

In a first approximation, the displacements of the nodes' gravity centre along the tangent to the structure's front-side directions (*y*-direction and *z*-direction; Fig. 2) are considered negligible with respect to the displacements along the normal to the structure's front-side direction (*x*-direction). Each node is therefore assumed to move along the *x*-direction only.

The remote interactions account for the contact forces applied at the interfaces between cells or between a cell and the boulder. The formulation of the remote interactions assumes that the cells are laterally confined by the neighbouring cells and uniaxially loaded by the boulder or the front cells. The models used for the calculation of the remote interactions between two nodes or between the front nodes and the boulder are different for the following reasons.

First, during the impact, it is assumed that the contact surfaces between two cells do not evolve significantly. On the contrary, the contact surface between the boulder and the front cells evolves substantially. Consequently, contact forces between nodes are determined assuming that the contact surface is a plane. Thus, the remote interaction forces between cells are calculated using stress–strain relationships associated with both of the interacting cells. The contact forces between the front nodes and the boulder are calculated directly in terms of interaction forces – boulder displacement relationships, because no simple formulation for the evolution of the contact surface is available.

Second, dynamics is of paramount importance for interactions in the vicinity of the impact point, i.e., for interactions between the front cells and the boulder (Fig. 2). On the other hand, for interactions between cells far from the impact point, the inertial effects are negligible, and the loading can be considered pseudo-static. As a consequence, the remote interaction models have been identified from dynamic experiments for interactions between the boulder and the front nodes, and from static experiments for interactions between nodes.

Remote interactions

Interactions between boulder and front nodes

In the *x*-direction, the increment $\mathrm{d}\boldsymbol{F}_i^{\mathrm{n}}$ of the normal interaction force $\boldsymbol{F}_i^{\mathrm{n}}$ applied by the boulder to the node *i* associated with a front cell is related with the displacement increment $\mathrm{d}u_i$, including the strain increments of the boulder and the cell *i* (Fig. 3):

$$[1] \qquad \mathrm{d}\boldsymbol{F}_i^{\mathrm{n}} = \frac{k_i^{\mathrm{g}} k^{\mathrm{b}}}{k_i^{\mathrm{g}} + k^{\mathrm{b}}} \mathrm{d}u_i \, \boldsymbol{x}$$

where k_i^{g} and k^{b} are the stiffness of the front cell *i* and the boulder, respectively, $\boldsymbol{x}$ is the unit vector associated with the *x*-direction, and

$$[2] \qquad \mathrm{d}u_i = \mathrm{d}x_r - \mathrm{d}x_i$$

where $\mathrm{d}x_r$ and $\mathrm{d}x_i$ are the increments of the displacements of the boulder and the node *i*, respectively, in the *x*-direction (Fig. 3).

Equation [1] can be rewritten as follows:

$$[3] \qquad \mathrm{d}\boldsymbol{F}_i^{\mathrm{n}} = \frac{k_i^{\mathrm{g}}}{1 + (k_i^{\mathrm{g}}/k^{\mathrm{b}})} \mathrm{d}u_i \, \boldsymbol{x}$$

As $k^{\mathrm{b}} >> k_i^{\mathrm{g}}$, eq. [3] can be simplified to

$$[4] \qquad \mathrm{d}\boldsymbol{F}_i^{\mathrm{n}} = k_i^{\mathrm{g}} \, \mathrm{d}u_i \, \boldsymbol{x}$$

The stiffness k_i^{g} is determined from the boulder – front-cell interaction model (Fig. 2) which is characterized by the function f_i^{F} relating the force applied on the cell by the boulder and the boulder penetration u_i

Fig. 3. Definition of the displacements of the gravity centre of the boulder (x_r), front cell i (x_i), and kernel cell j (x_j). These displacements are used for the calculation of the strains of front and kernel cells.

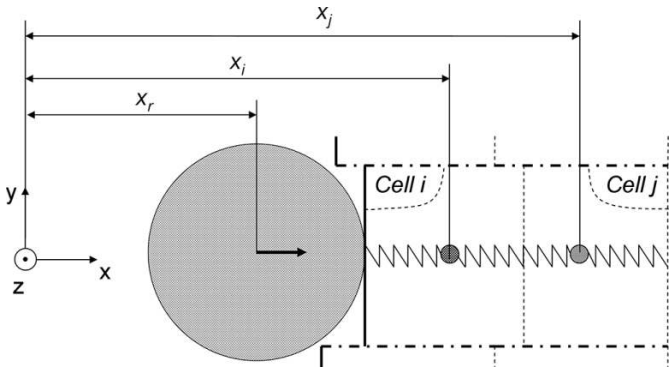

$$[5] \qquad k_i^{\mathrm{g}} = \frac{\partial f_i^{\mathrm{F}}}{\partial u_i}$$

If the impact velocity of the boulder is not normal to the front side of the structure or if the boulder's rotational velocity is not nil, a tangential force $\boldsymbol{F}_i^{\mathrm{t}}$ is also applied to the boulder at the contact point and the impacted front node. The tangential force $\boldsymbol{F}_i^{\mathrm{t}}$ accounts for the changes in the boulder's tangential and rotational velocities during the impact. $\boldsymbol{F}_i^{\mathrm{t}}$ is calculated following a Coulomb friction model

$$[6] \qquad \boldsymbol{F}_i^{\mathrm{t}} = -\mu_i^{\mathrm{F}} ||\boldsymbol{F}_i^{\mathrm{n}}|| \frac{\boldsymbol{V}_{\mathrm{b}}(C)}{||\boldsymbol{V}_{\mathrm{b}}(C)||}$$

where $\boldsymbol{V}_{\mathrm{b}}(C)$ is the tangent component of the velocity of the contact point C associated with the boulder in relation to the cell i and μ_i^{F} is the friction coefficient associated with the interaction between the boulder and the front cells.

Impact experiments (Lambert et al. 2009) were used to characterize the boulder – front-cell interaction mechanisms embedded in the function f_i^{F}. These experiments considered the impact by a spherical boulder on cells located above a concrete support.

The confinement conditions of the cells are highly variable, depending on the location of the cell in the structure. In our approach, two limit cases of confining conditions were explored. The lateral boundary conditions of the impacted cells (Fig. 4) were either free-to-deform (FD) or rigidly confined (RC). Real conditions are bounded by these two limit situations. Interaction models are first characterized for both of these confinement conditions and the more suitable model is chosen in the second stage by the comparative analysis of experimental and simulation results at the structure scale. For both confinement conditions, the interaction force between the boulder and the cell, the boulder's penetration, and the force transmitted to the concrete support were recorded.

The results from these experiments (Fig. 5*a*) allowed the definition of patterns of the function f_i^{F} depending on the lateral confinement of the cells (Fig. 5*b*).

During the loading phase ($\mathrm{d}u_i \geq 0$), for any confinement conditions and for penetrations smaller than the limit penetration, u^{lim}, the function f_i^{F} is characterized by a linear relation where k^{l} is the loading stiffness. For penetrations larger than u^{lim}, and for FD conditions only, the interaction force decreases when the penetration reaches the u^{lim} value to a lower value termed the limit force F^{pl}. For all confinement conditions, the unloading phase ($\mathrm{d}u_i < 0$) is characterized by a sharp linear decrease in the interaction force for decreasing penetrations where k^{ul} is the unloading stiffness.

For RC conditions, the incremental formulation of the boulder – front-cell interaction model is therefore: if $\mathrm{d}u_i \geq 0$, then

$$[7] \qquad \mathrm{d}F_i^{\mathrm{n}} = k^{\mathrm{l}}\,\mathrm{d}u_i$$

if $\mathrm{d}u_i < 0$, then

$$[8] \qquad \mathrm{d}F_i^{\mathrm{n}} = k^{\mathrm{ul}}\,\mathrm{d}u_i$$

For FD conditions, the boulder – front-cell interaction model can be expressed as follows: if $\mathrm{d}u_i \geq 0$ and $u_i < u^{\mathrm{lim}}$, then

$$[9] \qquad \mathrm{d}F_i^{\mathrm{n}} = k^{\mathrm{l}}\,\mathrm{d}u_i$$

if $\mathrm{d}u_i \geq 0$ and $u_i \geq u^{\mathrm{lim}}$, then

$$[10] \qquad F_i^{\mathrm{n}} = F^{\mathrm{pl}}$$

if $\mathrm{d}u_i < 0$, then

$$[11] \qquad \mathrm{d}F_i^{\mathrm{n}} = k^{\mathrm{ul}}\,\mathrm{d}u_i$$

The calibration of the different parameters associated with the function f_i^{F} will be detailed in the section titled "Impact simulations" (Table 1).

Interactions between cells

The force $\boldsymbol{F}_{i/j}^{\mathrm{n}}$, in the x-direction, applied by cell i to the cell j is calculated from the increment $\mathrm{d}\boldsymbol{F}_{i/j}^{\mathrm{n}}$ (Fig. 3)

$$[12] \qquad \mathrm{d}\boldsymbol{F}_{i/j}^{\mathrm{n}} = -\frac{S_{\mathrm{c}} E_{ij}}{d^0}\mathrm{d}u_{ij}\,\boldsymbol{x}$$

where d^0 is the distance between the nodes at the initial time-step and S_{c} is the area of the contact surface between the cells. $\mathrm{d}u_{ij}$ is the relative displacement of node i in relation to j

$$[13] \qquad \mathrm{d}u_{ij} = \mathrm{d}x_i - \mathrm{d}x_j$$

where $\mathrm{d}x_i$ and $\mathrm{d}x_j$ are the increments of the displacements of nodes i and j in the x-direction (Fig. 3). E_{ij} is the equivalent modulus accounting for both tangent moduli E_i and E_j associated with the nodes i and j

$$[14] \qquad E_{ij} = \frac{E_i E_j}{E_i + E_j}$$

The tangent moduli E_i and E_j are defined from constitutive models characterized by functions f_i^E and f_j^E relating the stress inside the cells to their strain. As the cell displacements only occur along the x-direction, the strain field within each cell has a single component ε_{xx}^i. The functions f_i^E and f_j^E can therefore be determined as follows:

$$[15] \qquad E_i = \frac{\partial f_i^E}{\partial \varepsilon_{xx}^i}$$

Fig. 4. Lateral boundary conditions used in the experiments: (*a*) free-to-deform (FD); (*b*) rigid confinement (RC) (adapted from Lambert et al. 2009).

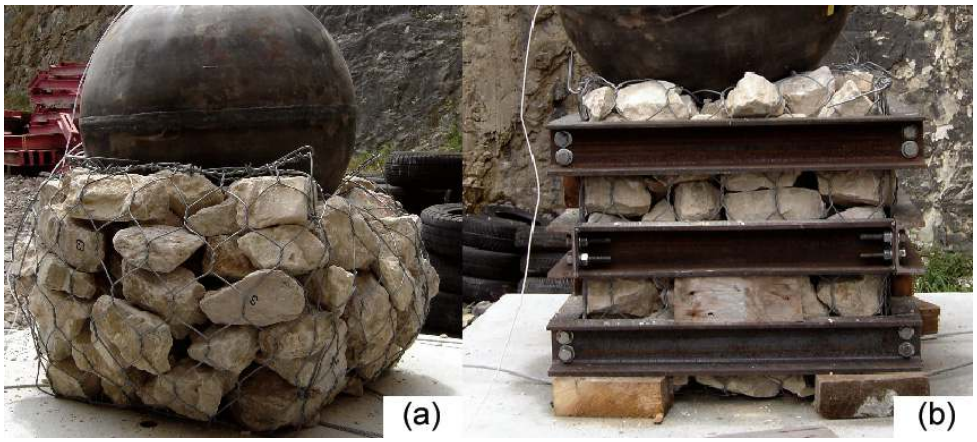

Fig. 5. (*a*) Experimental results of impacts on front-layer cells and (*b*) corresponding boulder – front-cell interaction models. F^{pl}, limit force; k^{l}, loading stiffness; k^{ul}, unloading stiffness.

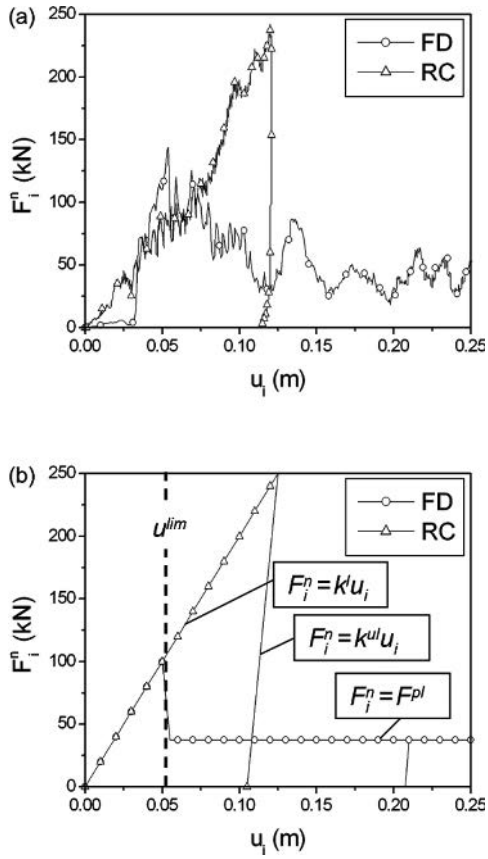

$$[16] \qquad E_j = \frac{\partial f_j^E}{\partial \varepsilon_{xx}^j}$$

Depending on the cell location, the tangent moduli E_i and E_j are determined using different constitutive models. Three types of constitutive models are used: front-cell constitutive models, kernel-cell constitutive models, and boundary constitutive models (Fig. 2).

Front-cell constitutive model

For the front-cell constitutive models, the modulus E_i is expressed using stress–strain relationships from static compression tests (Lambert 2007). Similar to the boulder – front-cell interaction models, the confinement conditions of the cells were either rigid (RC) or free-to-deform (FD) (Fig. 6). For the loading phase, the axial stress σ_{xx}^i at the cell interface in the x-direction, depending on the cell's axial strain ε_{xx}^i in the x-direction, is characterized by a linear increase in stress (Fig. 6). This relation is valid for both confinement conditions until the threshold value ε^{lim} is reached. For FD conditions and for ε_{xx}^i greater than ε^{lim}, the stress σ_{xx}^i remains equal to σ^{lim}. On the other hand, no threshold value is observed for RC conditions. Interestingly, the slope of the linear relation is different depending on the confinement conditions (Fig. 6): E_{rc}^{l} (for RC conditions) and E_{fd}^{l} (for FD conditions). The unloading phase is characterized by a linear decrease of σ_{xx}^i for decreasing ε_{xx}^i using the coefficient E_{rc}^{ul} for RC conditions and E_{fd}^{ul} for FD conditions (Fig. 6). The values of the different parameters used in the simulations are reported in Table 1.

For RC conditions, the incremental formulation of the front-cell constitutive model is: if $d\varepsilon_{xx}^i \geq 0$, then

$$[17] \qquad d\sigma_{xx}^i = E_{rc}^{l}\, d\varepsilon_{xx}^i$$

if $d\varepsilon_{xx}^i < 0$, then

$$[18] \qquad d\sigma_{xx}^i = E_{rc}^{ul}\, d\varepsilon_{xx}^i$$

For FD conditions, the incremental formulation of the front-cell constitutive model is: if $d\varepsilon_{xx}^i \geq 0$, then

$$[19] \qquad d\sigma_{xx}^i = E_{fd}^{l}\, d\varepsilon_{xx}^i \xi(\sigma^{lim} - \sigma_{xx}^i)$$

where ξ is the Heaviside function: $\xi(x) = 1$ if $x > 0$ and $\xi(x) = 0$ if $x \leq 0$. If $d\varepsilon_{xx}^i < 0$, then

$$[20] \qquad d\sigma_{xx}^i = E_{fd}^{ul}\, d\varepsilon_{xx}^i$$

Kernel-cell constitutive model

For the kernel-cell constitutive models, one can consider, in a first approximation, that the cells are loaded along a

Table 1. Parameters used in the structure model and their range of variation.

Model	Condition	Parameters	Value or variation range
Front-cell interaction	FD	Loading stiffness, k^{l}	2.8×10^6 N/m
		Unloading stiffness, k^{ul}	2.8×10^7 N/m
		Limit penetration, u^{lim}	0.075 m
		Limit force, F^{pl}	40 kN
	RC	Loading stiffness, k^{l}	2.8×10^6 N/m
		Unloading stiffness, k^{ul}	2.8×10^7 N/m
Front-cell constitutive	FD	Loading modulus, $E^{\mathrm{l}}_{\mathrm{fd}}$	5.5 MPa
		Unloading modulus, $E^{\mathrm{ul}}_{\mathrm{fd}}$	55 MPa
		Limit strain, $\varepsilon^{\mathrm{lim}}$	4%
	RC	Loading modulus, $E^{\mathrm{l}}_{\mathrm{rc}}$	16 MPa
		Unloading modulus, $E^{\mathrm{ul}}_{\mathrm{rc}}$	160 MPa
Kernel-cell constitutive	—	Loading modulus, $E^{\mathrm{l}}_{\mathrm{ke}}$	1 MPa $\leq E^{l}_{ke} \leq$ 100 MPa
	—	Unloading modulus, $E^{\mathrm{ul}}_{\mathrm{ke}}$	$E^{l}_{ke} \leq E^{ul}_{ke} \leq 10E^{l}_{ke}$
Boundary constitutive	—	Elastic modulus, E_{bo}	200 000 MPa
Lateral interaction	Front cells	Diffusion coefficient, K_i	$0 \leq K_i \leq 0.5$
		Friction angle, φ	$\varphi = 45°$
	Kernel cells	Diffusion coefficient, K_i	$0 \leq K_i \leq 0.5$
		Friction angle, φ	$\varphi = 30°$

Fig. 6. Front-cell constitutive models determined from static compression tests.

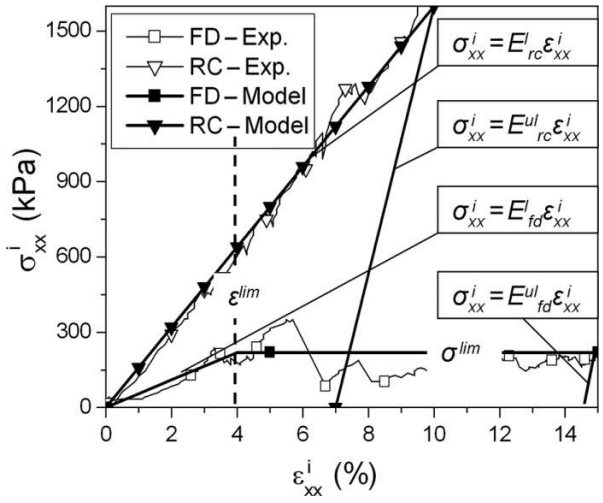

nearly oedometric path. A constant value of the loading modulus $E^{\mathrm{l}}_{\mathrm{ke}}$ is defined due to the lack of relevant experimental results in relation to the complexity of the lateral confinement conditions. A larger unloading modulus $E^{\mathrm{ul}}_{\mathrm{ke}}$ is also defined to account for the plastic strains observed during oedometric tests on sands. Values of the loading modulus $E^{\mathrm{l}}_{\mathrm{ke}}$ ranging from 1 to 100 MPa will be used in the simulations presented here to account for a wide range of sand density (Table 1). The influence of the ratio between the loading and the unloading moduli ($E^{\mathrm{ul}}_{\mathrm{ke}}/E^{\mathrm{l}}_{\mathrm{ke}}$) will also be studied for $1 \leq E^{\mathrm{ul}}_{\mathrm{ke}}/E^{\mathrm{l}}_{\mathrm{ke}} \leq 10$ (Table 1).

The incremental formulation of the kernel cells constitutive model is: if $\mathrm{d}\varepsilon^i_{xx} \geq 0$, then

$$[21] \qquad \mathrm{d}\sigma^i_{xx} = E^{\mathrm{l}}_{\mathrm{ke}}\,\mathrm{d}\varepsilon^i_{xx}$$

if $\mathrm{d}\varepsilon^i_{xx} < 0$, then

$$[22] \qquad \mathrm{d}\sigma^i_{xx} = E^{\mathrm{ul}}_{\mathrm{ke}}\,\mathrm{d}\varepsilon^i_{xx}$$

Boundary constitutive model

Finally, for the boundary constitutive models, the back part of the structure is modelled by a linear elastic model characterized by the elastic modulus E_{bo}, which depends on the embankment material. The incremental formulation of the kernel-cell constitutive model is

$$[23] \qquad \mathrm{d}\sigma^i_{xx} = E_{\mathrm{bo}}\,\mathrm{d}\varepsilon^i_{xx}$$

In the simulations, the back part is modelled as a concrete support (Table 1).

Lateral force model

The lateral diffusion inside the cellular structure of the energy transmitted by the projectile is related mainly to the lateral (y- and z-direction) cell strains induced by the cell strain in the x-direction. To account for this phenomenon, the assumption is made that, in the y- and z-directions, the cell i applies a force to the cell j (Fig. 7) related to the forces applied to the cell i in the x-direction (Nicot et al. 2007) with a normal component $\boldsymbol{F}^{\mathrm{n}}_{i/j}$ and a tangential component $\boldsymbol{F}^{\mathrm{t}}_{i/j}$

$$[24] \qquad \boldsymbol{F}^{\mathrm{n}}_{i/j} = K_i \max(||\boldsymbol{F}^{\mathrm{n},-}_i||, ||\boldsymbol{F}^{\mathrm{n},+}_i||)\,\boldsymbol{t}$$

where $\boldsymbol{F}^{\mathrm{n},-}_i$ (respectively $\boldsymbol{F}^{\mathrm{n},+}_i$) is the normal force applied on the front (respectively back) side of the cell i, K_i is a constant coefficient, and $\boldsymbol{t}$ is the unit vector associated with the y- or z-direction. The influence of the coefficient K_i will be explored in detail for K_i ranging from 0 to 0.5 (Table 1).

The tangential component $\boldsymbol{F}^{\mathrm{t}}_{i/j}$ is related to $\boldsymbol{F}^{\mathrm{n}}_{i/j}$ and $\boldsymbol{F}^{\mathrm{t}}_{j/i}$

$$[25] \qquad \boldsymbol{F}^{\mathrm{t}}_{i/j} = -\tan(\varphi)\max(||\boldsymbol{F}^{\mathrm{n}}_{i/j}||, ||\boldsymbol{F}^{\mathrm{n}}_{j/i}||)\left(\frac{\boldsymbol{V}_{i/j}}{||\boldsymbol{V}_{i/j}||}\right)$$

where φ is the Coulomb friction angle associated with the cells i and j and $\boldsymbol{V}_{i/j}$ is the relative velocity of the cell i in relation to the cell j. φ was set at $\varphi = 45°$ for front cells and $\varphi = 30°$ for kernel cells (Table 1).

Fig. 7. Definition of $F^{t}_{i/j}$, $F^{n}_{i/j}$, $F^{n}_{j/i}$, $F^{n,-}_{i}$, and $F^{n,+}_{i}$ forces.

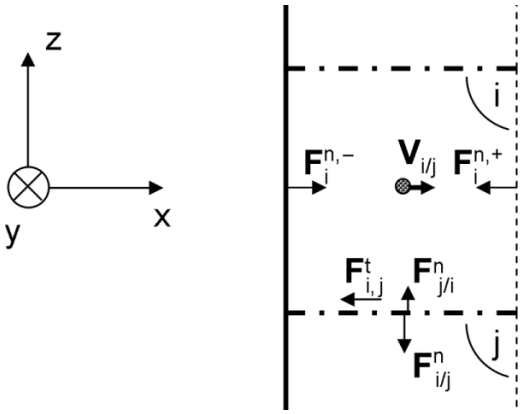

Impact simulations

Impacts on single cells

Simulations of impact experiments at the cell scale (Lambert et al. 2009) are first considered to calibrate the parameters of the interaction model between the boulder and the front cells. For these simulations, the structure model is reduced to a single node (Fig. 8) that models a front-layer cell in front of a concrete support. A spherical projectile impacts the structure normal to the front face with an incident velocity $V^{in} = 10.4$ m/s. The mass of the projectile is 262 kg. Simulations of impacts on cells under FD and RC confinement conditions are performed. The parameters used for the front-cell constitutive models and for the boundary constitutive models are set with the values defined in the previous section (Table 1).

The experimental results of the impact force for FD confinement conditions are first used to calibrate all the parameters of the boulder – front-cell interaction models for both FD and RC confinement conditions (Fig. 9). The values obtained during this calibration phase are summarized in Table 1.

The transmitted forces measured in the experiments are used in the second phase for validation purposes. The comparison between the experimental and the simulation results shows that the model can predict the experimental results (Fig. 10). The correct prediction of the maximum values reached by the transmitted forces (4% and 18% differences for RC and FD conditions, respectively) is useful for design purposes. In addition, the agreement between the experimental and simulated time evolutions of all forces (Fig. 10) shows that the model proposed simulates the main characteristics of the dynamic interactions between the boulder, the cell, and the support. However, the model does not reproduce the fast variations observed on the experimental curves resulting from stone crushing (Lambert et al. 2009).

The simulation of impacts on front-layer cells determined the values of all parameters associated with the boulder – front-cell interaction model (Table 1). In addition, static compression tests were used to determine the parameters associated with the front-cell constitutive model (Table 1), and friction angles associated with the lateral forces model are set at values inside classical ranges of variation for gravels and sands (Bardet 1998).

However, using the structure model for design purposes also requires choosing between FD and RC conditions for the interaction and constitutive models associated with front-layer cells. The use of the structure model also requires characterizing the parameters of the kernel-layer cell constitutive model (E^{l}_{ke} and E^{ul}_{ke}) and the coefficients K_i associated with the lateral force model. As no relevant values from the literature or from additional experiments at the cell scale are available to characterize these parameters, comparisons between experiments at the structure scale and simulation using the structure model will be reported in the following section to provide additional information for the complete characterization of the parameters of the structure model.

Impacts on structures

Impact experiments at the structure scale were also simulated to evaluate the consistency of the structure model by comparative analyses with experimental results. The methodology followed in this section consists of performing simulations of the experiments for different values of the loading modulus of the kernel cells E^{l}_{ke}, the E^{ul}_{ke}/E^{l}_{ke} ratio between the unloading and the loading modulus of the kernel cells, and the coefficients K_i for both front and kernel cells.

Impact experiments on a structure

The experiments consisted of subjecting a two-layered sandwich structure to pendulum impacts (Heymann et al. 2010). The impacted structure was 1.5 m high, 2.5 m long, and 1 m thick (Fig. 11). The front of the structure was composed of 15 cubic cells, 500 mm in height. The fill material was a crushed quarry limestone, 80 to 150 mm in grain size. The kernel of the structure consisted of a 50 cm thick sand cushion. The sand was well graded with a grain size ranging from 0.2 to 5 mm. This material was dumped bulk in a geotextile between the front layer and a concrete wall reinforced by a ground-compacted embankment.

The projectile consisted of a spherical boulder weighing 262 kg, 54 cm in diameter. This boulder was suspended above the structure using two cables. The maximum release height of the projectile was 4.75 m above the soil. The impact point was centered on the front of the structure. The structure was impacted, successively increasing the impact energy. The investigated energies were 2, 4, 8, and 10 kJ.

The projectile acceleration was measured using a triaxial piezoresistive accelerometer. Accelerations within the structure were measured in the impact direction in the middle of the kernel layer and at the interface between the front layer and the kernel layer, using uniaxial piezoresistive accelerometers. Finally, the force transmitted to the concrete wall was measured using sensors with a sensitive surface of 0.1 m^2.

The results presented are the impact force F^{imp} (Fig. 12) and the normal stresses on the wall, σ^{tran}_{F1} and σ^{tran}_{F4}, respectively, measured in the impact direction and 50 cm from the impact vertical plane on the same horizontal plane (Figs. 11, 13).

Impact simulations at the structure scale

The complete model presented in the section titled "Numerical model" was used for the simulations of the impact experiments at the structure scale. As the confinement conditions provided by the material surrounding each cell are situated between FD and RC conditions, preliminary simulations were required to evaluate which of the constitutive models

Fig. 8. Model used for the simulations of impact experiments on a front-layer cell.

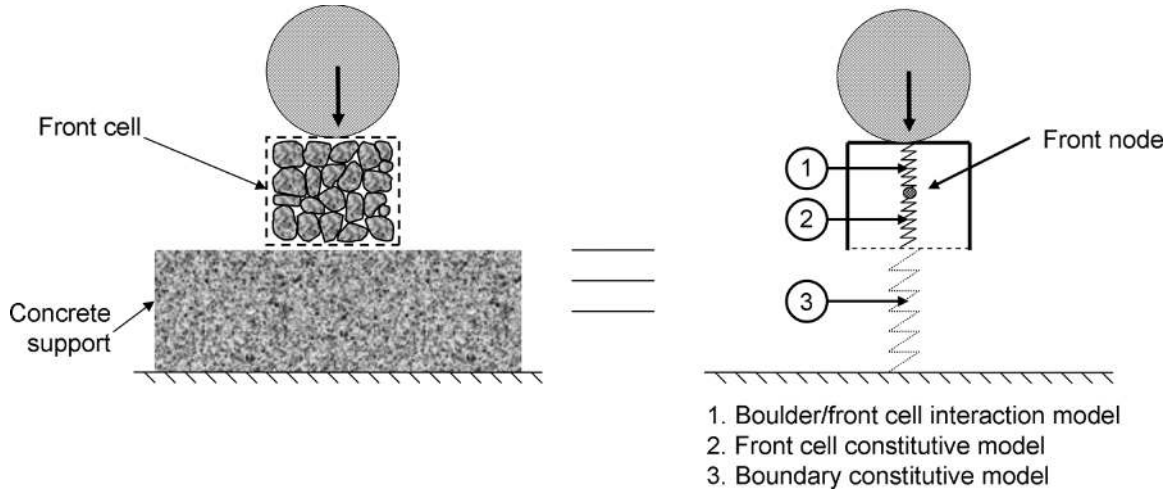

Fig. 9. Calibration of the boulder – front-cell interaction models for both (*a*) FD and (*b*) RC conditions using the impact force measured during impact experiments. Exp., experiment; sim., simulation.

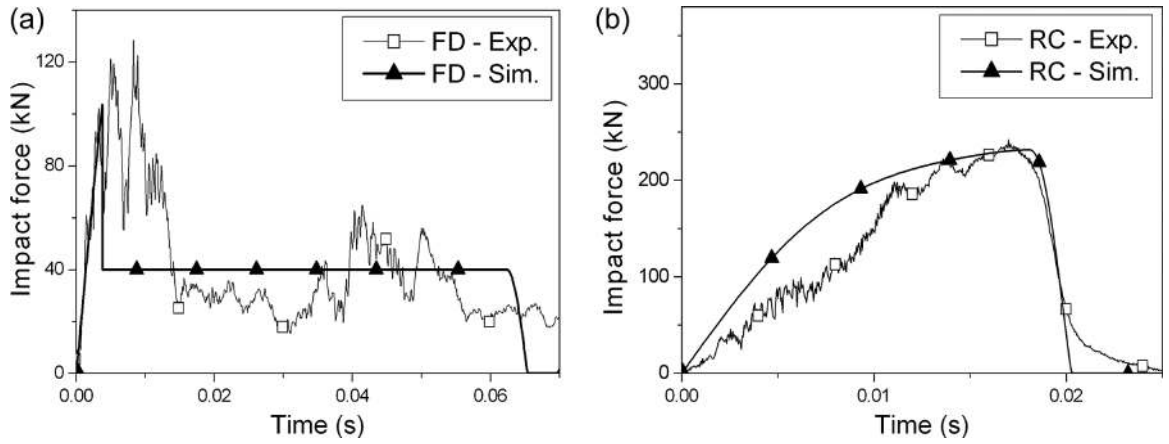

Fig. 10. Comparison between the experimental and simulation results for the force transmitted to the support using cells in both (*a*) FD and (*b*) RC conditions.

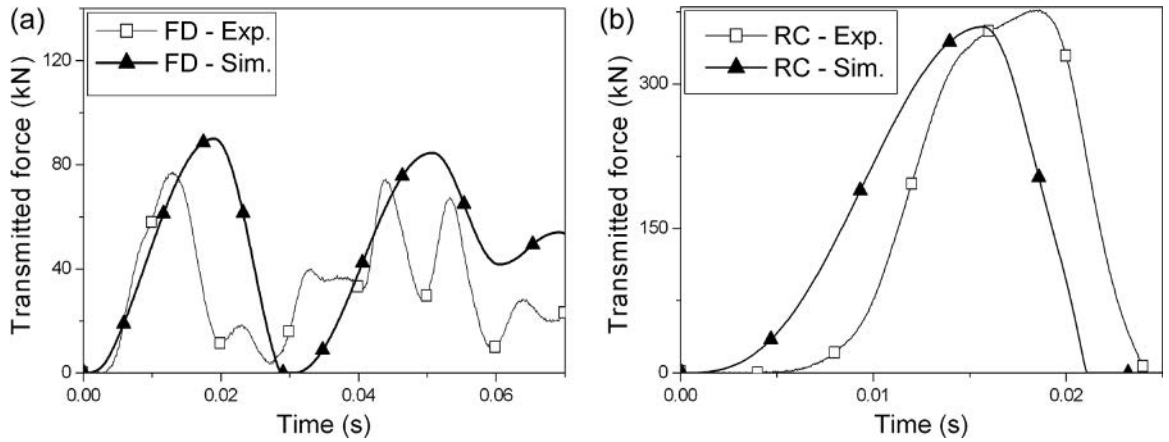

associated with RC or FD confinement conditions is the most suitable for real confinement conditions.

Second, a sensitivity analysis was carried out to evaluate the influence of the loading modulus E_{ke}^{l}, the E_{ke}^{ul}/E_{ke}^{l} ratio, and the coefficients K_i on the simulation results. The parameters concerned varied within the following ranges: 1 MPa $\leq E_{ke}^{l} \leq$ 100 MPa, $1 \leq E_{ke}^{ul}/E_{ke}^{l} \leq 10$, and $0 \leq K_i \leq 0.5$ (Table 1). In all simulations, when the influence of each of these parameters was not explored, they were set at $E_{ke}^{l} = 10$ MPa, $E_{ke}^{ul}/E_{ke}^{l} = 3$, $K_i^{front} = 0.25$, $K_i^{kernel} = 0.25$.

In the experiments, impact tests at increasing energies were carried out on the same structure, whereas in the simulations,

Fig. 11. Experimental device used in the experiments of impact on a structure. An accelerometer (a_1) was placed in the projectile and two stress sensors (F_1 and F_4) were located on the rear side of the structure behind the kernel cells C_1 and C_4.

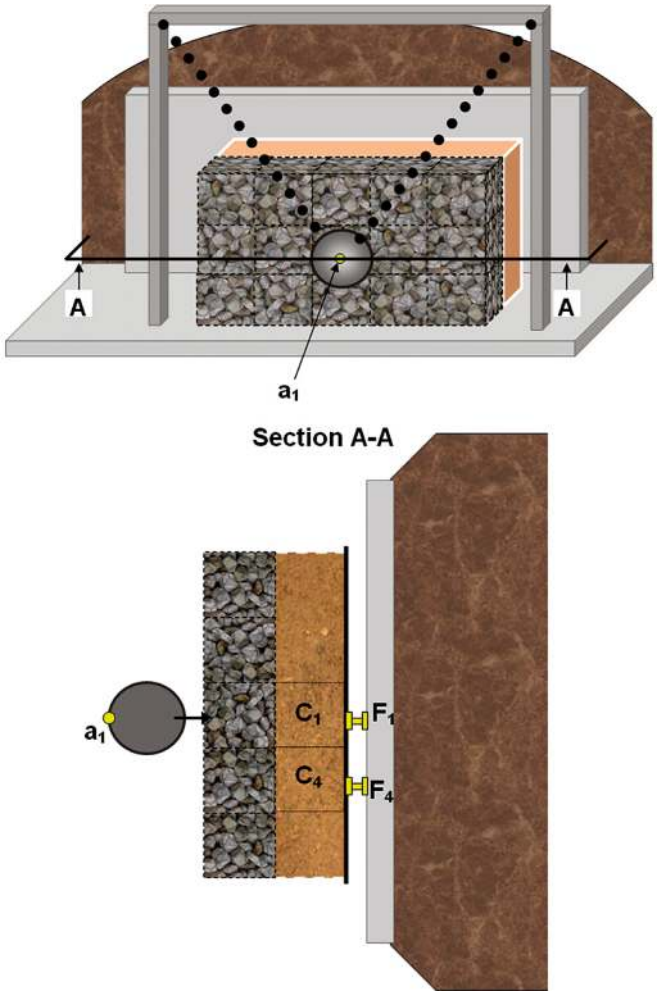

Fig. 12. Impact force, F^{imp}, measured in the experiments.

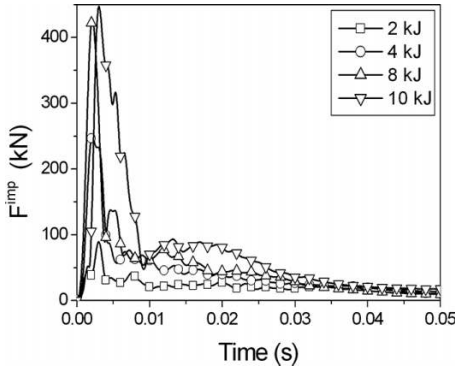

the structure was different for each impact simulation. The choice was made not to include the effects of successive impacts in the structure model in the first stage. Indeed, it would significantly increase the complexity of the model. In particular, for repeated impacts on the same structure, the shapes of the lateral interaction surfaces between adjoining cells evolve from planar surfaces to curved surfaces. As the

Fig. 13. Transmitted stresses (*a*) σ_{F1}^{tran} and (*b*) σ_{F4}^{tran} measured in the experiments.

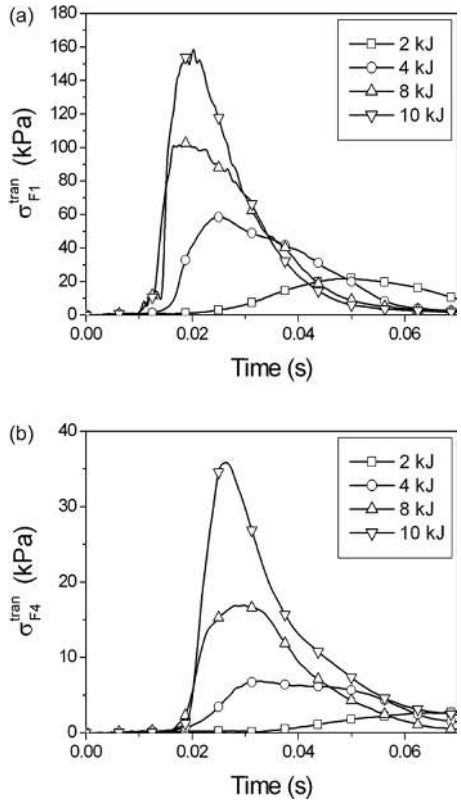

shearing between cells differs greatly for planar surfaces and curved surfaces, modelling structure damage would entail defining, in particular, the changes from one impact to the following in the relationship between the forces $\boldsymbol{F}_{i/j}^{n}$, $\boldsymbol{F}_{i}^{n,-}$, and $\boldsymbol{F}_{i}^{n,+}$, not a trivial task.

Influence of the confinement conditions

The effect of the confinement conditions is first studied by simulating impacts of different impact energies for front cells in both RC and FD confinement conditions. In these simulations, $E_{ke}^{l} = 10$ MPa, $E_{ke}^{ul}/E_{ke}^{l} = 3$, $K_i^{front} = 0.25$, $K_i^{kernel} = 0.25$. The simulations clearly show that the confinement conditions strongly influence the impact force on the projectile in terms of both time evolution and maximum value (Fig. 14). However, differences between models associated with FD and RC conditions are only observed for energies greater than 2 kJ, i.e., for energies great enough for F^{imp} to reach the limit impact force F^{lim}. For this range of energy, one can observe that FD conditions induce smaller maximum forces and longer contact — the contact being associated with a non-nul impact force — durations between the structure and the boulder.

Using models based on FD conditions does not allow fitting of the experimentally observed increase in the impact force for increasing impact energy (Figs. 12, 14*a*). Constitutive models associated with FD conditions are therefore not suitable in terms of prediction of the maximum impact force.

Models associated with RC conditions provide more relevant predictions of the maximum impact force, in particular for low-impact energies (Figs. 12, 14*b*, 15). Differences are

Fig. 14. Impact force, F^{imp}, using front-cell constitutive models associated with (*a*) FD and (*b*) RC conditions for different impact energies (Ec^{imp}).

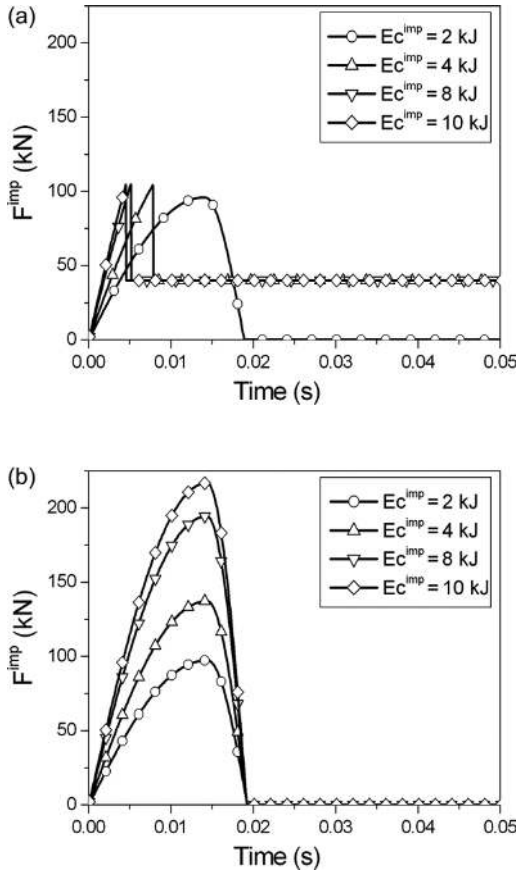

observed, however, due to the cumulative damage from one impact to another in the experimental structure, which is not accounted for in the simulations. Differences are also observed in the time evolution of the forces in the simulations and experiments (Figs. 12, 14*b*, 15). First, the main peak of the impact force occurs sooner in the experiments than in the simulations (Fig. 15). Second, after the main peak, the impact force vanishes directly in the simulations, whereas a slow decrease is observed in the experiments. The differences in the occurrence of the main peak may be explained by the differences in terms of granulometry and stone resistance between the fill material of the front cells in the experiments at the structure scale and in the experiments at the cell scale used for calibration of the model. In addition, as the vertical displacements of the structure are not accounted for in the simulations, differences can be observed during the decreasing phase of the impact force. Indeed, during the decreasing phase of the impact force in the experiments, the boulder stops penetrating the structure and starts falling down. The front-layer cells that were deformed by the impact also start falling down, which is not accounted for in the model. Consequently, an interaction may occur between the projectile and the front-layer cells that are vertically moving, which is not accounted for in the simulation.

Despite the differences observed, the models associated with RC conditions provide relevant results for the main peak of the contact force, i.e., for the main energy exchanges.

Fig. 15. Comparison of the impact force F^{imp} between the experiments and the simulation using front-cell constitutive models assuming RC conditions for impact energies equal to (*a*) 2 kJ and (*b*) 8 kJ.

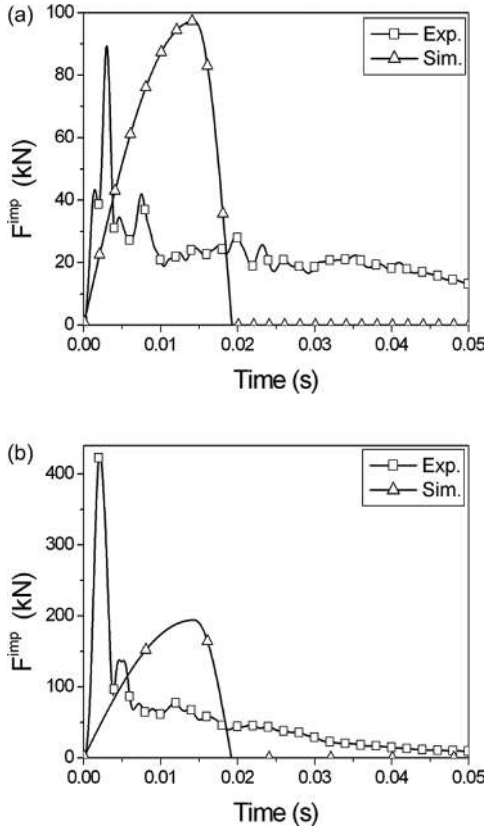

The correct prediction of the energy exchanges is considered as the most important criterion, therefore the models associated with RC conditions are used in the following.

Influence of the kernel cells moduli E^{l}_{ke} and E^{ul}_{ke}

To limit the effects of structure damage in the experiments compared with the simulations, the analysis of the influence of the kernel-cell moduli is undertaken for impact energies set at 4 kJ. Indeed, for higher energies the damage is too great, while for lower energy values, the forces and stresses measured are too small.

For the analysis of the influence of the loading modulus E^{l}_{ke}, interaction and constitutive models associated with RC conditions were chosen for front cells. The K_i coefficients were set at $K_i^{front} = 0.25$ and $K_i^{kernel} = 0.25$, and E^{ul}_{ke}/E^{l}_{ke} was set at 3. Different values for the loading modulus E^{l}_{ke} were used, ranging from 1 to 100 MPa.

For increasing values of the loading modulus of the kernel cells E^{l}_{ke}, the impact force increases only slightly (Fig. 16*a*). Indeed, the increase in the loading modulus of the kernel layer entails an increase in the global stiffness of the structure, which results in an increase in the interaction force between the structure and the boulder. The stiffness of the kernel cells also strongly influences the time evolution of the transmitted stresses (Fig. 17). As loading modulus E^{l}_{ke} increases, the duration of the loading on the rear side of the structure decreases and the maximum transmitted stresses in-

Fig. 16. Impact force, F^{imp}, for different loading moduli of (*a*) the kernel-layer cells E^{l}_{ke} and (*b*) ratio E^{ul}_{ke}/E^{l}_{ke}.

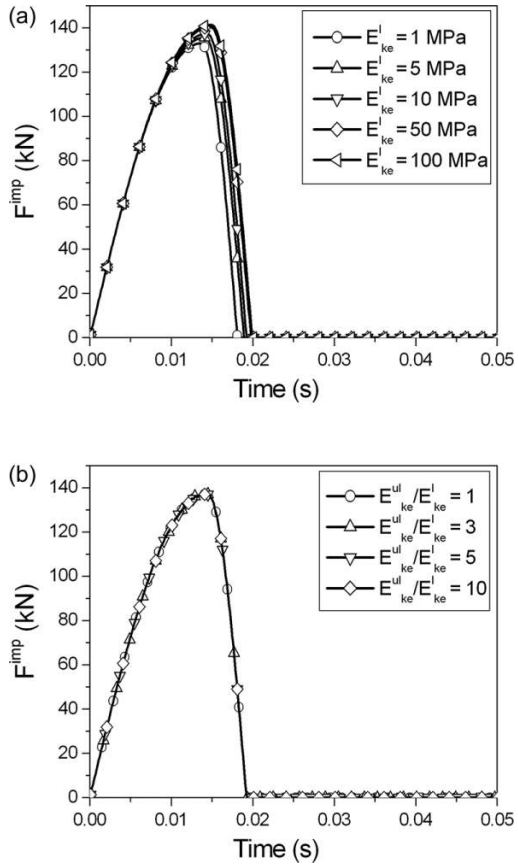

Fig. 17. Transmitted stresses (*a*) σ^{tran}_{F1} and (*b*) σ^{tran}_{F4} for different loading moduli of the kernel-layer cells E^{l}_{ke}.

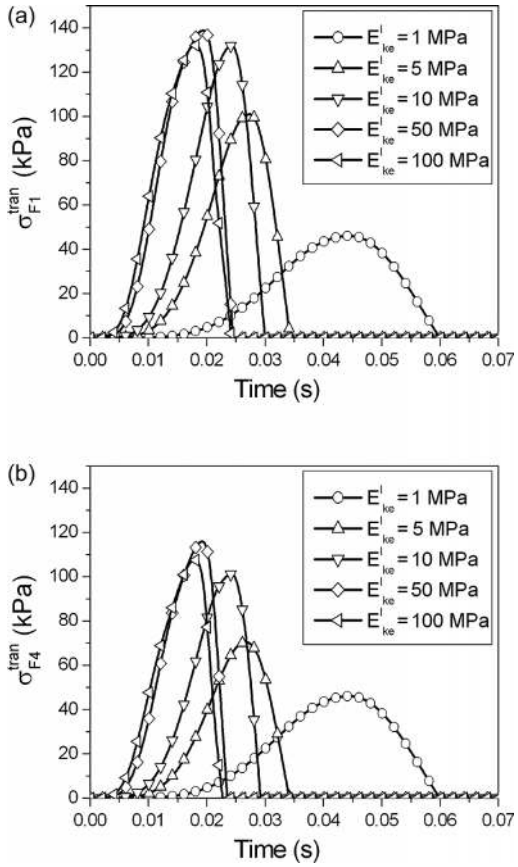

crease. Similarly, the experimental results show that, as impact energy increases, the loading duration decreases and the maximum transmitted stresses increase (Fig. 13). This similar evolution shows that repeated impacts at increasing energies alter the loading modulus of the kernel-layer cells. Indeed, the successive impacts induce compaction of the kernel layer and, consequently, an increase in the kernel-layer modulus.

The value of the ratio between the loading and the unloading modulus, E^{ul}_{ke}/E^{l}_{ke}, does not influence the impact force (Fig. 16*b*). Noting that the stress at the interface between the front and kernel cells starts decreasing for durations longer than 0.02 s (Fig. 18) for which the impact force has already vanished (Fig. 16*b*), one can deduce that the unloading of the kernel cells occurs after the vanishing of the impact force. As the value of the E^{ul}_{ke} ratio only acts during the unloading of the kernel cells, the observed independence of the impact force on the ratio E^{ul}_{ke}/E^{l}_{ke} is consistent. The influence of the ratio E^{ul}_{ke}/E^{l}_{ke} is only significant on the transmitted stresses σ^{tran}_{F1} and σ^{tran}_{F4} (Fig. 19). The increase in the ratio E^{ul}_{ke}/E^{l}_{ke} produces larger plastic strains in the kernel-layer material, that is larger energy dissipation inside the cells, which results in decreasing transmitted stresses σ^{tran}_{F1} and σ^{tran}_{F4}.

Influence of the diffusion coefficients K_i

As for the analysis of the kernel cells moduli, the study of the influence of the diffusion coefficients K_i was done for impact energies set at 4 kJ. For the analysis of the influence of the coefficients K^{front}_i and K^{kernel}_i, constitutive models associated with RC conditions were chosen for the front cells. The loading modulus of the kernel cells and the ratio E^{ul}_{ke}/E^{l}_{ke} were set at E^{l}_{ke} = 10 MPa and E^{ul}_{ke}/E^{l}_{ke} = 3. Both coefficients K^{front}_i and K^{kernel}_i were chosen equal ($K^{front}_i = K^{kernel}_i = K_i$) and different values of K_i were explored.

Fig. 18. Stress at the interface between the front and the kernel cells, $\sigma^{tran}_{front/cell}$, for different ratios of E^{ul}_{ke}/E^{l}_{ke}.

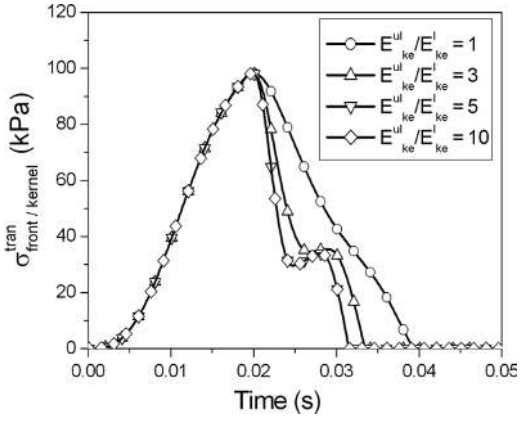

The coefficients K_i account for the diffusion of the energy transmitted to the cell considered. For increasing values of K_i, more cells are involved in transmitting the impact energy through the whole structure. As a result, the global resistance of the structure is increased (Fig. 20): the impact force increases with K_i.

Fig. 19. Transmitted stresses (*a*) σ_{F1}^{tran} and (*b*) σ_{F4}^{tran} for varying ratios of E_{ke}^{ul}/E_{ke}^{l}.

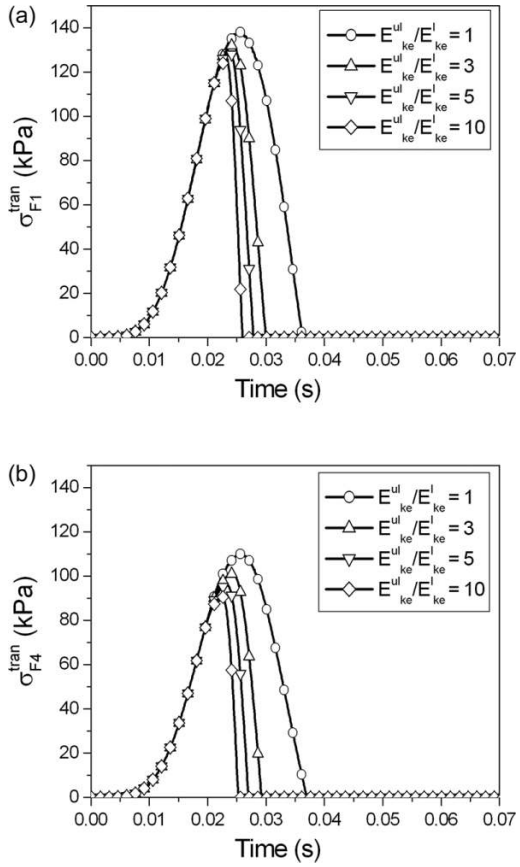

Fig. 20. Impact force, F^{imp}, for different values of the coefficients K_i^{front} and K_i^{kernel}.

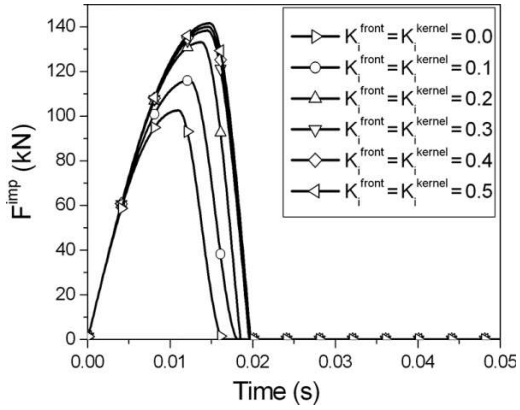

In addition, the simulations show that the increase in the coefficients K_i entails a decrease in the transmitted stresses σ_{F1}^{tran} (Fig. 21*a*). Indeed, for low values of K_i, the cell C_1 (Fig. 11) is the only cell transmitting the impact energy. For increasing values of K_i, the number of cells involved in the impact energy transmission increases, which decreases the stress transmitted by the cell C_1.

The changes in the transmitted stresses σ_{F4}^{tran} in terms of the coefficient K_i values is more complex (Fig. 21*b*). σ_{F4}^{tran} is nil for $K_i = 0$, increases until K_i reaches 0.2, and decreases when K_i is higher than 0.2. This complex behaviour is related to

Fig. 21. Transmitted stresses (*a*) σ_{F1}^{tran} and (*b*) σ_{F4}^{tran} for different values of the coefficients K_i^{front} and K_i^{kernel}.

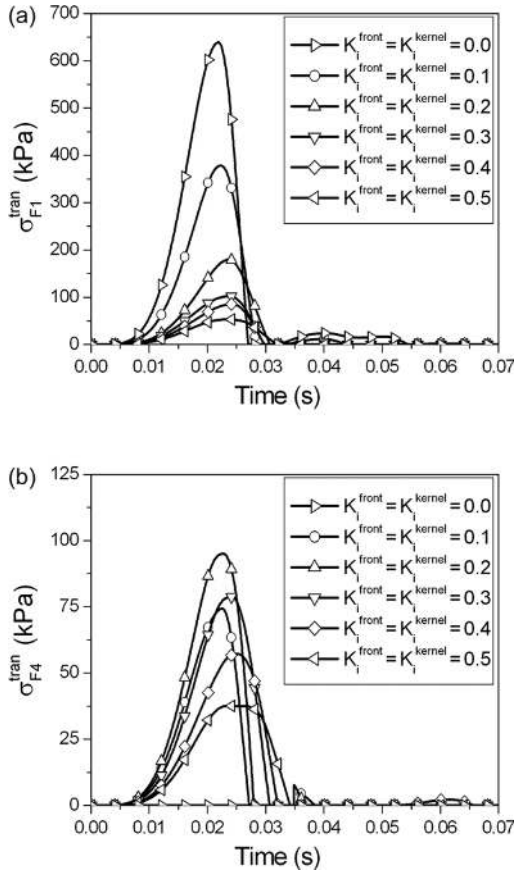

the location of the force sensor F_4. As the force sensor F_4 is located 50 cm from the impact direction, it is not loaded if diffusion is not considered, i.e., if $K_i = 0$. When K_i increases, the shear forces $\boldsymbol{F}_{i/j}^{t}$ applied on the cell C_4 by the adjoining kernel cell C_1 (Fig. 11), in particular, also increase. The strain of cell C_4 (Fig. 11) therefore increases, which induces an increase in the transmitted stress σ_{F4}^{tran}. However, when K_i reaches high values ($K_i = 0.2$, Fig. 21*b*), the cells located farther from the impact point than cell C_4 are also loaded. The transmitted energy is therefore divided into a larger number of cells, which tends to decrease the stress transmitted by cell C_4.

Conclusions and perspectives for the use of the model in engineering practice

The approach presented throughout this paper was developed for engineering purposes. To this aim, a set of simple constitutive models was developed for the different parts of the structure, through a multi-scale approach. The good agreement observed between the experimental and numerical results proves the relevance of this approach and shows that the main physical mechanisms appear to have been accounted for. In particular, the simulations at the structure scale highlight the potential of the model for the design of rockfall protection structures.

The design of rockfall protection structures consists of assessing the efficiency of the structure to stop the rocks and of

quantifying the damage induced by the impact. Assessing the efficiency of the structure requires analysing the evolution of the rock trajectory to determine whether the rock is stopped or not. The characterization of the damage induced by the impact is different, depending on the part of the structure considered. Rockfall protection structures (in particular, cellular structures) are designed so that the front part of the structure allows dissipation of the impact energy. In addition, the rear part of the structure is designed to prevent the structure from being completely destroyed after impact. Consequently, the front part is composed of highly deformable materials and the rear part is a rigid structure in which plastic strains have to be limited. The damages on the structure are therefore related to both the deformation of the front part and the intensity of the stresses on the rear part of the structure.

The model developed can first provide relevant information on the capacity of the structure to stop the rock. Indeed, the trajectory of the rocks is explicitly calculated during the impact. However the calculated rock trajectories can only be used as initial estimates due to the assumptions associated with the calculation of the interactions between the rock and the structure.Although the incidence angle and the rotational velocity of the rock are accounted for, the tangential interaction forces between the rock and the structure are modelled using a simple Coulomb friction model. In addition, impacts at the boundary between two cells cannot be modelled.

The model can also provide quantitative information on the damages on the front and rear parts of the structure. The deformation of the front face can be assessed using the evolution of the boulder penetration depth during impact. In addition, the model allows calculating the evolution of the stresses applied on the rear part of the structure, which can then be used to estimate the potential plastic strains. One can note that the time evolution of all these quantities can be used as loading cases for detailed design of the structure using complex numerical approaches based on the finite element method (Ronco et al. 2009) or a discrete element method (Plassiard and Donzé 2010).

Depending on the effort put into the calibration of the model, the model can either be used as a preliminary design tool to determine the general layout of the structure and the materials composing the different layers or as a quantitative design model.

Using the model as a preliminary design tool can provide information on the global sizes of the structure and on the materials in the different layers. For that purpose, the calibration effort may be reduced based on constitutive models and experiments from the literature. Simulations for different values of the parameters of the constitutive models extracted from possible ranges of variation allow determination of the general structure layout, and the material composing each layer. For a specific type of structure, general design and building guidelines can therefore be determined based on simulations results using the model as a preliminary design tool.

Using the model as a quantitative design tool requires performing intensive experiments at the cell scale to determine the constitutive models for the different layers and the values of the associated parameters. The results obtained at the structure scale emphasize that defining a clear procedure for calibrating the model is possible. Indeed, the simulation results have shown that each output of the model —time evolution or maximum values of the impact force or the transmitted stresses — can be used to calibrate the parameters introduced in the simulation.

It is worth noting that this model constitutes a powerful, simplified quantitative design tool compared with complex models based on the finite element method (Ronco et al. 2009) or on a discrete element method (Plassiard and Donzé 2010). The main advantage of the model compared with these approaches is its computational efficiency. Due the relative simplicity of the model compared with these approaches, the simulation of a simple impact is much faster. Such a model can therefore be considered as a compromise between empirical or analytical design approaches and design methodologies based on complex numerical simulations. Consequently, detailed analysis of the influence of the assumed parameters for the structure can be done using this model in a reasonable and practical time frame. In addition, the computational efficiency of the model also allows the possibility for the performance of reliability analyses for the structure. Reliability analyses are based on the statistical analysis of numerous impact simulations under varying impact conditions and structure parameters. They allow characterization of the probability of failure of the structure or the probability that a rock will not be be stopped depending on the variability of the impact conditions and the material parameters. Accounting for the variability of the mechanical parameters used to describe the structure through a stochastic approach could therefore be regarded as a useful perspective for this work, in line with stochastic modelling of the rockfall trajectory recently carried out by Bourrier et al. (2009*a*, 2009*b*).

Acknowledgements

This research was funded by the French National Research Agency (ANR) within the "Re-Ingénièrie des Merlons de Protection par composants Anthropiques REcyclés" (REMPARe) project. It was developed within the framework of the "Vulnérabilité des Ouvrages aux Risques" (VOR–RNVO) research consortium. The authors wish to acknowledge all the partners of the project, especially Razel SA, the Road Experimentation Centre (CER) in Rouen, and Elizabeth Haza-Rozier for carrying out the experimental tests.

References

Aminata, D., Yashima, A., Sawada, K., Sung, E., Sugimori, K., and Inoue, S. 2008. New protection wall against rockfall using a ductile cast iron panel. Journal of Natural Disaster Science, **30**(1): 25–33. doi:10.2328/jnds.30.25.

Bardet, J.P. 1998. Introduction to computational granular mechanics. *In* Behaviour of granular materials. *Edited by* B. Cambou. Springer Wien, New York. pp. 99–169.

Bertrand, D., Nicot, F., Gotteland, P., and Lambert, S. 2005. Modelling a geo-composite cell using discrete analysis. Computers and Geotechnics, **32**(8): 564–577. doi:10.1016/j.compgeo.2005.11.004.

Blovsky, S. 2002. Model tests on protective barriers against rockfall. *In* Proceedings of the 15th EYGEC – European Young Geotechnical Engineers Conference, Dublin, Ireland, 11–14 September 2002.

Bourrier, F., Eckert, N., Nicot, F., and Darve, F. 2009*a*. Bayesian stochastic modeling of a spherical rock bouncing on a coarse soil.

Natural Hazards and Earth System Sciences, **9**(3): 831–846. doi:10.5194/nhess-9-831-2009.

Bourrier, F., Dorren, L., Nicot, F., Berger, F., and Darve, F. 2009*b*. Towards objective rockfall trajectory simulation using a stochastic impact model. Geomorphology, **110**(3–4): 68–79. doi:10.1016/j.geomorph.2009.03.017.

Burroughs, D., Henson, H.H., and Jiang, S.S. 1993. Full scale geotextile rock barrier wall testing, analysis and prediction. *In* Proceedings of Geosynthetics 93, Vancouver, B.C, 30 March – 1 April 1993. Industrial Fabrics Association Internationa (IFAI), St. Paul, Minn. pp. 959–970.

Calvetti, F., Di Prisco, C., and Vecchiotti, M. 2005. Experimental and numerical study of rock-fall impacts on granular soils. Rivista Italiana di Geotecnica, **4**: 95–109.

Carotti, A., Di Prisco, C., Vecchiotti, M., Recalcati, P., and Rimoldi, P. 2004. Modeling of geogrid reinforced embankments for rockfall protection. *In* Proceedings of the 3rd European Geosynthetics Conference, Munich, Germany, 1–3 March 2004. pp. 675–680.

Cundall, P.A., and Strack, O.D.L. 1979. A discrete numerical model for granular assemblies. Géotechnique, **29**(1): 47–65. doi:10.1680/geot.1979.29.1.47.

Gotteland, P., Lambert, S., and Balachowski, L. 2005. Strength characteristics of tyre chips-sand mixtures. Studia Geotechnica et Mechanica, **27**: 55–66.

Hearn, G., Barrett, R.K., and Henson, H.H. 1995. Development of effective rockfall barriers. Journal of Transportation Engineering, **121**(6): 507–516. doi:10.1061/(ASCE)0733-947X(1995)121:6(507).

Heymann, A., Lambert, S., Haza-Rozier, E., Vinceslas, G., and Gotteland, P. 2010. An experimental comparison of half-scale rockfall protection sandwich structures. *In* Proceedings of Structures under Shock and Impact XI -SUSI XI, Tallinn, Estonia, 28–30 July 2010. Witpress, Southampton, UK.

Jaecklin, F. 2006. Innovative design for repairing Gondo mudslide by 20m high geogrid wall. *In* Proceedings of the 8th International Conference on Geosynthetics, Yokohama, Japan, 18–22 September 2006. Millpress Science Publishers, Rotterdam, the Netherlands. pp. 1223–1228.

Labiouse, V., Descoeudres, F., Montani, S., and Schmidtaler, C.-A. 1994. Etude expérimentale de la chute de blocs rocheux sur une dalle en béton armée recouverte par des matériaux amortissants. Revue Française de Géotechnique, **69**: 41–62.

Lambert, S. 2007. Mechanical behaviour of geocells with application to cellular rock-fall protection dykes components. Ph.D. thesis, Joseph Fourier, Grenoble, France. [In French.]

Lambert, S., Gotteland, P., and Nicot, F. 2009. Experimental study of the impact response of geocells as components of rockfall protection embankments. Natural Hazards and Earth System Sciences, **9**(2): 459–467. doi:10.5194/nhess-9-459-2009.

Montani Stoffel, S. 1998. Sollicitation dynamique de la couverture des galeries de protection lors de chutes de blocs. Ph.D. thesis, École Polytechnique Fédérale de Lausanne (EPFL), Lausanne, Switzerland.

Nicot, F., Gotteland, P., Bertrand, D., and Lambert, S. 2007. Multi-scale approach to geo-composite cellular structures subjected to rock impacts. International Journal for Numerical and Analytical Methods in Geomechanics, **31**(13): 1477–1515. doi:10.1002/nag.604.

Peila, D., Oggeri, C., and Castiglia, C. 2007. Ground reinforced embankments for rockfall protection: design and evaluation of full scale tests. Landslides, **4**(3): 255–265. doi:10.1007/s10346-007-0081-4.

Peila, D., Castiglia, C., Oggeri, C., Guasti, G., Recalcati, P., and Rimoldi, P. 2002. Testing and modelling geogrid reinforced soil embankments subject to high energy rock impacts. *In* Proceedings of the 7th International Conference on Geosynthetics, Nice, France, 22–27 September 2002. Swets and Zeilinger, Amsterdam, the Netherlands. pp. 133–136.

Pichler, B., Hellmich, C., Eberhardsteiner, J., and Mang, H.A. 2005. Assessment of protection systems for buried steel pipelines endangered by rockfall. Computer-Aided Civil and Infrastructure Engineering, **20**(5): 331–342. doi:10.1111/j.1467-8667.2005.00400.x.

Plassiard, J.-P., and Donzé, F. 2010. Optimizing the design of rockfall embankments with a discrete element method. Engineering Structures, **32**(11): 3817–3826. doi:10.1016/j.engstruct.2010.08.025.

Ronco, C., Oggeri, C., and Peila, D. 2009. Design of reinforced ground embankments used for rockfall protection. Natural Hazards and Earth System Sciences, **9**(4): 1189–1199. doi:10.5194/nhess-9-1189-2009.

Schellenberg, K., Volkwein, A., Denk, M., and Vogel, T. 2008. Falling weight tests on rock fall protection galleries with cushion layers. *In* Proceedings of the Interdisciplinary Workshop on Rockfall Protection, Morschach, Switzerland, 23–25 June 2008. *Edited by* A. Volkweinn, V. Labiouse, and K. Schellenberg. pp. 99–101.

Sung, E., Yashima, A., Aminata, D., Sugimori, K., Sawada, K., Inoue, S., and Nishida, Y. 2007. Numerical assessment of the performance of protecting wall against rockfall. *In* Proceedings of the 5th International Symposium on Earth Reinforcement, Kyushu, Japan, 14–16 November 2007. Taylor and Francis, London. pp. 861–867.

Tissières, P. 1999. Ditches and reinforced ditches against falling rocks. *In* Proceedings of the Joint Japan–Swiss Scientific Seminar on Impact Load by Rockfalls and Design of Protection Structures, Kanazawa, Japan, 4–7 October 1999. *Edited by* H. Masuya and V. Labiouse. pp. 65–68.

Yoshida, H. 1999. Recent experimental studies on rockfall control in Japan. *In* Proceedings of the Joint Japan–Swiss Scientific Seminar on Impact by Rock Falls and Design or Protection Structures, Kanazawa, Japan, 4–7 October 1999. *Edited by* H. Masuya and V. Labiouse. pp. 69–78.